Electronic Supporting Information

Contrast Mechanisms on Nanoscale Subsurface Imaging in Ultrasonic AFM: Scattering of Ultrasonic Wave and Contact Stiffness of Tip-Sample

Hossein Jiryaei Sharahi,[a] Gajendra Shekhawat,[b] Vinayak Dravid,[b] Simon Park,[a] Philip Egberts[a] and Seonghwan Kim* [a]

[a]Department of Mechanical and Manufacturing Engineering, University of Calgary, AB, Canada.

*E-mail: sskim@ucalgary.ca

[b]Department of Materials Science and Engineering Northwestern University, IL, USA.

Contents

1) Effect of the contact stiffness on wave scattering

The wave scattering displacements after incident with a nano-feature can be determined using equation (7) in the paper. The coefficients of this equation depend on the wavenumbers in the sample matrix and the nano-feature that are related to the longitudinal and shear wave velocities. These wavenumbers are:

$$\alpha_{\mathrm{i}}^2 = \frac{\omega^2 \rho_{\mathrm{i}}}{\lambda_{\mathrm{i}}+2\mu_{\mathrm{i}}}, \beta_{\mathrm{i}}^2 = \frac{\omega^2 \rho_{\mathrm{i}}}{\lambda_i} \quad \text{(S-1)}$$

where i=1 denotes the sample matrix and i=2 represents the nano-feature. The Lame's constants, λ and μ, are related by shear modulus (G) and bulk modulus (K) as: $\lambda = K - \frac{2}{3}G$ and μ = G. Therefore, the ultrasonic scattering response depends on the bulk modulus, shear modulus and density of the sample matrix and the nano-feature. Given that the maximum applied force on the tip is in order of few tens nN for soft materials (such as polymer) and a few hundred nN for hard materials and no evidence of plastic deformation was observed in previous experimental measurements[1,2], we can limit our analysis to elastic deformation. Assuming elastic deformation means that the mechanical properties of both the tip and substrate, such as elastic and shear moduli, will not be affected. However, the local density of the material in the vicinity of the tip-sample contact when compressed will increase. To gain insight into the influence of the variation of local density of the sample on the wave scattering response, we calculated the local variation of the PS volume and consequently the local variation of PS density beneath the AFM tip. Using the FEM simulations to measure the contact radius and indentation depth under an applied load of 100 nN, it was determined that they were 15 nm and 1.3 nm, respectively. Under these

conditions, the local density of the substrate increased approximately 7%. This 7% variation in local density changes the phase contrast of ultrasonic wave scattering by 3.5%. It can be concluded the maximum contribution of contact stiffness on ultrasonic wave scattering is less than 3.5% for soft materials. This influence of the contact stiffness on wave scattering may also have effect on the linear superposition of these two mechanisms, therefore the discrepancy between experimental data and theoretical results can be discussed by this explanation as well.

2) Effect of the wave scattering on contact stiffness

To understand the influence of the ultrasonic wave scattering on contact stiffness contrast, the Hertzian theory for contact stiffness can be discussed. Based on this model, the contact stiffness is defined as[3]:

$$k^* = \sqrt[3]{6F_0RE^{*2}} \quad \text{(S-2)}$$

where F_0 is applied force, R is the tip radius, and E^* is the effective Young's modulus of the tip (E_t & ν_t) and the sample (E_s & ν_s) that is obtained by:

$$\frac{1}{E^*} = \frac{1-\nu_t^2}{E_t} + \frac{1-\nu_s^2}{E_s} \quad \text{(S-3)}$$

Then, the contact stiffness mainly depends on the geometry of the AFM tip, tip radius, applied force on tip, and Poisson ratio and Young's modulus in the tip and the sample. So, to determine the effect of the wave scattering on contact stiffness, we need to check the frequency dependence of Young's modulus of the sample. The relation between Young's modulus and frequency in polymer can be estimated by[4]:

$$E = A\ \log_{10} f + B\ (10^{10}\ \text{dyne/cm}^2) \quad \text{(S-4)}$$

where A, and B are constant values that can be estimated experimentally for a specific material. For example, in PS these values can be estimated as 0.037 and 3.32, respectively[4]. By considering these values and changing the frequency up to 5 MHz, the variation in Young's modulus was 8%. This variation in Young's modulus of polymer was applied in FEA simulation and the variation in contact stiffness (Δk) was calculated. FEA simulation has been done on a PS sample that includes a gold nanoparticle with 50 nm radius embedded 60 nm under the sample. Figure S1 schematically shows two polymer matrixes with different Young's modulus. The contact stiffness variation due to the nanoparticle for PS (E) was calculated equal to $\Delta\mathrm{k} = 2.16\frac{\mathrm{N}}{\mathrm{m}}$, while it was equal to $\Delta\mathrm{k} = 2.25\frac{\mathrm{N}}{\mathrm{m}}$ for PS (E+8%E). Then, the variation of contact stiffness due to the 5 MHz ultrasonic wave is equal to: $\Delta\mathrm{k}\% = \frac{2.25-2.16}{2.16} = 4\%$. Since the phase will be affected linearly with contact stiffness, it is expected the contribution of wave scattering on contact stiffness will be around 4% for PS at 5 MHz excitation signal. The discrepancy between experimental and theoretical results can be explained by this explanation as well.

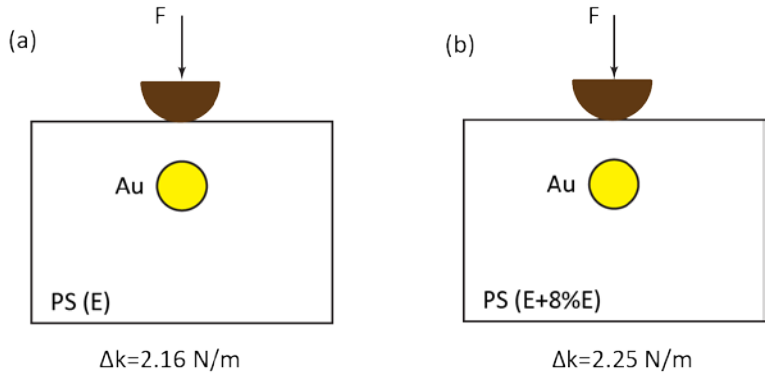

Figure S1- The contact stiffness variation due to the (a) gold nanoparticle (b) summation of the gold nanoparticle and 8% change in Young's modulus of polymer.

3) Boundary conditions for the cavity and elastic inclusion in wave scattering mechanism

For an elastic nano-feature, boundary conditions are determined using continuity of stresses and displacements at the interface of elastic nano-feature and polymer, in which r=a (radius of sphere). These conditions give:

$$\begin{bmatrix} E_{11,\mathrm{n}} & E_{12,\mathrm{n}} & E_{13,\mathrm{n}} & E_{14,\mathrm{n}} \\ E_{21,\mathrm{n}} & E_{22,\mathrm{n}} & E_{23,\mathrm{n}} & E_{24,\mathrm{n}} \\ E_{31,\mathrm{n}} & E_{32,\mathrm{n}} & PE_{33,\mathrm{n}} & PE_{34,\mathrm{n}} \\ E_{41,\mathrm{n}} & E_{42,\mathrm{n}} & PE_{43,\mathrm{n}} & PE_{44,\mathrm{n}} \end{bmatrix} \begin{bmatrix} A_n \\ B_n \\ C_n \\ D_n \end{bmatrix} = \Phi_0 \begin{bmatrix} E_{1,\mathrm{n}} \\ E_{2,\mathrm{n}} \\ E_{3,\mathrm{n}} \\ E_{4,\mathrm{n}} \end{bmatrix} \tag{S-5}$$

where $E_{\mathrm{i,n}} = \varepsilon_{\mathrm{i,n}}$, $E_{\mathrm{ij,n}} = \varepsilon_{\mathrm{ij,n}}$ at r=a. The symbols, $\varepsilon_{ij,n}$ in Eq. (S-5), linear combinations of the spherical harmonics, are defined as:

$$\begin{cases} \varepsilon_{1,\mathrm{n}} = -i^n(2n+1)(nj_n(\alpha_1 r) - \alpha_1 r j_{n+1}(\alpha_1 r),\ \varepsilon_{2,\mathrm{n}} = -i^n(2n+1)j_n(\alpha_1 r) \\ \varepsilon_{3,\mathrm{n}} = -i^n(2n+1)[(n^2 - n - \frac{1}{2}\beta_1^2 r^2)j_n(\alpha_1 r) + 2\alpha_1 r j_{n+1}(\alpha_1 r)] \\ \varepsilon_{4,\mathrm{n}} = -i^n(2n+1)[(n-1)j_n(\alpha_1 r) - \alpha_1 r j_{n+1}(\alpha_1 r)] \\ \varepsilon_{11,\mathrm{n}} = nh_n(\alpha_1 r) - \alpha_1 r h_{n+1}(\alpha_1 r)\,, \varepsilon_{21,\mathrm{n}} = h_n(\alpha_1 r) \\ \varepsilon_{31,\mathrm{n}} = \left(n^2 - n - \frac{1}{2}\beta_1^2 r^2\right) h_n(\alpha_1 r) + 2\alpha_1 r h_{n+1}(\alpha_1 r) \\ \varepsilon_{41,\mathrm{n}} = (n-1)h_n(\alpha_1 r) - \alpha_1 r h_{n+1}(\alpha_1 r) \\ \varepsilon_{12,\mathrm{n}} = -n(n+1)h_n(\beta_1 r),\ \varepsilon_{22,\mathrm{n}} = -(n+1)h_n(\beta_1 r) + \beta_1 r h_{n+1}(\beta_1 r) \\ \varepsilon_{32,\mathrm{n}} = -n(n+1)[(n-1)h_n(\beta_1 r) - \beta_1 r h_{n+1}(\beta_1 r)] \\ \varepsilon_{42,\mathrm{n}} = -\left(n^2 - 1 - \frac{1}{2}\beta_1^2 r^2\right) h_n(\beta_1 r) - \beta_1 r h_{n+1}(\beta_1 r) \\ \varepsilon_{13,\mathrm{n}} = nj_n(\alpha_2 r) - \alpha_2 r j_{n+1}(\alpha_2 r)\,, \varepsilon_{23,\mathrm{n}} = j_n(\alpha_2 r) \\ \varepsilon_{33,\mathrm{n}} = \left(n^2 - n - \frac{1}{2}\beta_2^2 r^2\right) j_n(\alpha_2 r) + 2\alpha_2 r j_{n+1}(\alpha_2 r) \\ \varepsilon_{43,\mathrm{n}} = (n-1)j_n(\alpha_2 r) - \alpha_2 r j_{n+1}(\alpha_2 r) \\ \varepsilon_{14,\mathrm{n}} = -n(n+1)j_n(\beta_2 r),\ \varepsilon_{24,\mathrm{n}} = -(n+1)j_n(\beta_2 r) + \beta_2 r h_{n+1}(\beta_2 r) \\ \varepsilon_{34,\mathrm{n}} = -n(n+1)[(n-1)j_n(\beta_2 r) - \beta_2 r j_{n+1}(\beta_2 r)] \\ \varepsilon_{44,\mathrm{n}} = -\left(n^2 - 1 - \frac{1}{2}\beta_2^2 r^2\right) j_n(\beta_2 r) - \beta_2 r j_{n+1}(\beta_2 r) \end{cases} \tag{S-6}$$

Eq. (S-5) shows that A_n and B_n depend on Bessel and Hankel functions in which their arguments are a function of *ka*, where *k* is wave number and *a* is the nano-feature radius. In our paper, the wave number in case of polymer and 1 MHz frequency is $\sim 10^3$ m^{-1} and the nano-feature radius is $\sim 10^{-7}$ m. Since

$ka \sim 10^{-4} \ll 0.1 \ll 1$, we are in the Rayleigh scattering regime[5]. In this regime, A_n and B_n can be explicitly evaluated as a close approximation. This approximation only neglects higher order of ka as:

$$j_n(ka) = \frac{2^n n!(ka)^2}{(2n+1)!}[1 + O(ka)^2] \quad \text{(S-7)}$$

$$h_n(ka) = \frac{2n!}{2^n n! i(ka)^{n+1}}[1 + O(ka)^2] \quad \text{(S-8)}$$

Unlike an elastic inclusion, for spherical cavity the boundary conditions will be simplified as the continuity of the stresses[6]:

$$\tau_r^{inc} + \tau_r^s = 0 \quad \text{(S-9)}$$

$$\tau_\theta^{inc} + \tau_\theta^s = 0 \quad \text{(S-10)}$$

where τ denotes stress for incident and scatter waves in r and θ directions. This yields two equations:

$$\begin{bmatrix} E_{31,\mathrm{n}} & E_{32,\mathrm{n}} \\ E_{41,\mathrm{n}} & E_{42,\mathrm{n}} \end{bmatrix} \begin{bmatrix} A_n \\ B_n \end{bmatrix} = \Phi_0 \begin{bmatrix} E_{3,\mathrm{n}} \\ E_{4,\mathrm{n}} \end{bmatrix} \quad \text{(S-11)}$$

Then, the coefficients A_n and B_n will be determined, and substituted in Eq. (7) in manuscript. To have a model with a minimum approximation and determine above mentioned coefficients with highest accuracy, we consider the two higher order terms of Bessel and Hankel functions and their series are solved numerically for the value of *n* up to 10. We have checked the convergence of our results for higher values of *n*, and higher order terms of Bessel and Hankel function. It was observed that the results are converged with less than 1% error.

4) The contribution of contact stiffness on phase contrast

In addition to phase contrast due to the ultrasonic wave scattering, a phase shift of ultrasonic-AFM happens from tip-sample interactions. To calculate this phase shift, the variation of contact stiffness (Δk^*) should be determined using Eq. (11) in the manuscript.

Then, an analytical model[7,8] was used to calculate the value of phase contrast resulting from the variation of contact stiffness. This model considered the cantilever and the sample as independent systems in which the interaction force provides a coupling between them. The solution of this pair of coupled nonlinear differential equations leads to contribution of contact stiffness on the phase contrast. The total phase factor can be determined as:

$$\Delta\varphi_{total} = \Delta\alpha + \Delta\beta + \Delta\varphi_s - \Delta\varphi_c - \Delta\varphi_{cs} \quad \text{(S-12)}$$

where

$$\Delta\alpha = -\left(\frac{\gamma_s\omega_c}{(k_s+k_e)^2+\gamma_s^2\omega_c^2}\right)\Delta k^* \quad \text{(S-13)}$$

$$\Delta\beta = -\left(\frac{\gamma_s\Delta\omega}{(k_s+k_e)^2+\gamma_s^2\Delta\omega^2}\right)\Delta k^* \quad \text{(S-14)}$$

$$\Delta\varphi_s = -\left(\frac{(\gamma_s k_{cr}^2+2k_e\gamma_s k_{cr}+k_e^2(\gamma_c+\gamma_s)\omega_s)+\left(\gamma_c^2\gamma_s-2\gamma_s m_c(k_{cr}+k_e)\right)\omega_s^3+m_c^2\gamma_s\omega_s^5}{\left((\gamma_c k_s+\gamma_s k_{cr}+k_e(\gamma_c+\gamma_s))\omega_s-\gamma_s m_c\omega_s^3\right)^2+\left((k_{cr}-m_c\omega_s^2+k_e)k_s+k_e\left(k_{cr}-m_c\omega_s^2\right)-\gamma_c\gamma_s\omega_s^2\right)^2}\right)\Delta k^* \quad \text{(S-15)}$$

$$\Delta\varphi_c = -\left(\frac{(\gamma_s k_{cq}^2+2k_e\gamma_s k_{cq}+k_e^2(\gamma_c+\gamma_s)\omega_c)+\left(\gamma_c^2\gamma_s-2\gamma_s m_c(k_{cq}+k_e)\right)\omega_c^3+m_c^2\gamma_s\omega_c^5}{\left(\left(\gamma_c k_s+\gamma_s k_{cq}+k_e(\gamma_c+\gamma_s)\right)\omega_c-\gamma_s m_c\omega_c^3\right)^2+\left((k_{cq}-m_c\omega_c^2+k_e)k_s+k_e(k_{cq}-m_c\omega_c^2)-\gamma_c\gamma_s\omega_c^2\right)^2}\right)\Delta k^* \quad \text{(S-16)}$$

$$\Delta\varphi_{cs} = -\left(\frac{(\gamma_s k_c^2+2k_e\gamma_s k_c+k_e^2(\gamma_c+\gamma_s)\Delta\omega)+\left(\gamma_c^2\gamma_s-2\gamma_s m_c(k_c+k_e)\right)\Delta\omega^3+m_c^2\gamma_s\Delta\omega^5}{\left(\left(\gamma_c k_s+\gamma_s k_c+k_e(\gamma_c+\gamma_s)\right)\Delta\omega-\gamma_s m_c\Delta\omega^3\right)^2+\left((k_c-m_c\Delta\omega^2+k_e)k_s+k_e(k_c-m_c\Delta\omega^2)-\gamma_c\gamma_s\Delta\omega^2\right)^2}\right)\Delta k^* \quad \text{(S-17)}$$

Where γ_s and γ_c are damping coefficients in the sample and the cantilever, respectively. The sample frequency, cantilever frequency, and their difference frequency are denoted by ω_s , ω_c , and $\Delta\omega$, respectively. The sample contact stiffness that is determined by FEA simulation was denotes by k_s , and k_c , and m_c represent the stiffness and mass of the cantilever. In above equations, the effective stiffness constant of the nonlinear interaction force, k_e, is used to obtain from the experimental tip-sample force curve. The k_{cr}, and k_{cq} are the cantilever stiffness constants corresponding to the r[th] and q[th] noncontact resonance modes of the cantilever having frequencies nearest ω_s and ω_c , respectively. The cantilever stiffness at higher-modes (k_{cn}) can be determined as[9,10]:

$$k_{cn} = \left(\frac{f_n}{f_0}\right)^2 k_c \quad \text{(S-18)}$$

where higher flexural resonant frequencies (f_n) for the rectangular cantilever can be obtained as[11]:

$$\frac{f_n}{f_0} = \left[\frac{c_n}{1.87}\right]^2, c_1 = 1.87, c_2 = 4.69, c_3 = 7.87, c_n \approx \frac{2n-1}{2}\pi \quad \text{(S-19)}$$

Based on the above equations, phase contrast ($\Delta\varphi_{total}$) has a linear dependence on variation of contact stiffness (Δk^*):

$$\Delta\varphi_{total} = K_{total}\Delta k^*$$

where K_{total} is a constant coefficient that is defined by material properties of the cantilever and the sample, as well as excitation frequencies. It is worth mentioning that analytical model includes the first-order term in the nonlinearity. This term is sufficient enough to account for the most important operational ultrasonic-AFM[7].

5) Dimension of the contact area as a function of the set force

Additional FEA simulations were performed to investigate the effect of the applied forces on the contact area using the FEA simulations described within the manuscript. Figure S2 shows the contact radius as a function of applied force. The FEA simulations have a gold nanoparticle, with a radius of 50 nm, embedded 60 nm in a PS matrix and a hemispherical tip of 150 nm. As it is expected, the higher applied force results bigger contact radius, and consequently higher contact stiffness. A best fit line has been drawn using a power function $Y = AX^B$ where A=2.72×10^{-6} and B=0.33. It is worth mentioning that this curve approximately follows the Hertzian contact theory where contact radius is defined as:

$$cr = \sqrt[3]{\frac{3F_0R}{4E^*}} \rightarrow cr = \left(\frac{3R}{4E^*}\right)^{\frac{1}{3}}(F_0)^{\frac{1}{3}} = (3.07\times10^{-6})\times(F_0)^{0.33} \quad \text{(S-20)}$$

where the discrepancy between the Hertzian theory and FEA is mainly due to the influence of the buried gold nanoparticle.

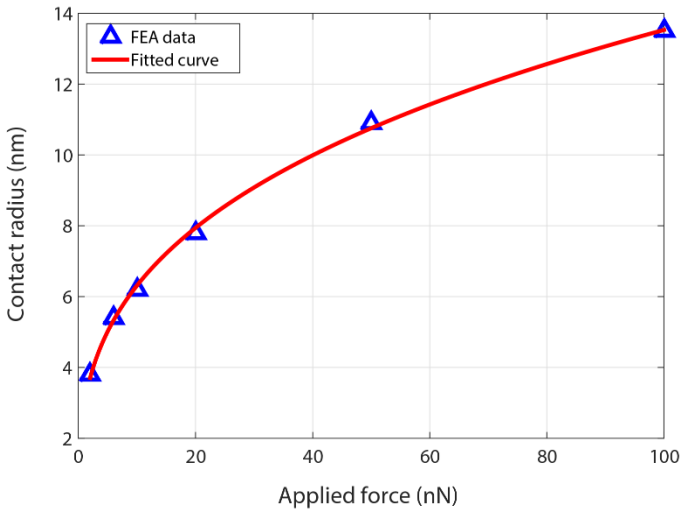

Figure S2- The contact radius as a function of applied forces for a PS sample that includes a gold nanoparticle with a radius of 50 nm embedded 60 nm under the sample surface.

References

1 J. P. Killgore, J. Y. Kelly, C. M. Stafford, M. J. Fasolka and D. C. Hurley, *Nanotechnology*, 2011, **22**, 175706.

2 Z. Parlak and F. L. Degertekin, *J. Appl. Phys.*, 2008, **103**, 114910.

3 K. L. Johnson and K. L. Johnson, *Contact Mechanics*, Cambridge University Press, 1987.

4 N. Lagakos, J. Jarzynski, J. H. Cole and J. A. Bucaro, *J. Appl. Phys.*, 1986, **59**, 4017.

5 A. N. Norris, *Int. J. Eng. Sci.*, 1986, **24**, 1271–1282.

6 Y.-H. Pao and C. C. Mow, *J. Appl. Phys.*, 1963, **34**, 493–499.

7 J. H. Cantrell and S. A. Cantrell, *Phys. Rev. B*, 2008, **77**, 165409.

8 S. A. Cantrell, J. H. Cantrell and P. T. Lillehei, *J. Appl. Phys.*, 2007, **101**, 114324.

9 A. Labuda, M. Kocun, T. Walsh, J. Meinhold, T. Proksch, W. Meinhold, M. Lysy and R. Proksch, *ArXiv Prepr. ArXiv160400601*, 2016.

10 J. Melcher, S. Hu and A. Raman, *Appl. Phys. Lett.*, 2007, **91**, 053101.

11 U. Rabe, in *Applied Scanning Probe Methods II*, Springer, 2006, pp. 37–90.